

# Robust Bulk Superconductivity by Giant Proximity Effect in Weyl Semimetal-superconducting NbP/NbSe<sub>2</sub> Composites

**Yejin Lee**

Kyung Hee University

**Omkaram Inturu**

Kyung Hee University

**Jin Hee Kim**

Kyung Hee University

**Jong-Soo Rhyee** (✉ [jsrhyee@khu.ac.kr](mailto:jsrhyee@khu.ac.kr))

Kyung Hee University

---

## Research Article

**Keywords:** NbP, NbSe<sub>2</sub>, Superconductivity, bulk composite, Weyl semimetal

**Posted Date:** September 21st, 2021

**DOI:** <https://doi.org/10.21203/rs.3.rs-890116/v1>

**License:**  This work is licensed under a Creative Commons Attribution 4.0 International License.

[Read Full License](#)

---

# Robust bulk superconductivity by giant proximity effect in Weyl semimetal-superconducting NbP/NbSe<sub>2</sub> composites

Yejin Lee<sup>†</sup>, Omkaram Inturu, Jin Hee Kim, Jong-Soo Rhyee\*

*Department of Applied Physics and Integrated Education Program for Frontier Science and Technology (BK21 Four), Institute of Natural Sciences, Kyung Hee University, Yong-In 17104, Republic of Korea*

## Abstract

We synthesize Weyl semimetal/superconductor NbP/NbSe<sub>2</sub> composite and observe stable bulk superconductivity at  $T_c = 7.2$  K, 6.9 K, and 6.8 K for NbSe<sub>2</sub> crystal, NbP/NbSe<sub>2</sub> (1:1), and NbP/NbSe<sub>2</sub> (2:1) composites, respectively, despite large volume fraction of non-superconducting NbP phase. From the Ginzburg-Landau theory, the  $H_{c2}(0)$  is significantly enhanced in NbP/NbSe<sub>2</sub> composites [22 T (1:1) and 18.5 T (2:1)] comparing with the pristine NbSe<sub>2</sub> crystal (8 T). The bulk superconductivity in Weyl semimetal/superconductor composite cannot be simply described by the de Gennes-Meissner theory in a proximity effect. From the electrical transport, magnetization, and heat capacity measurement, we obtain various superconducting parameters. The superconducting properties indicate that the NbP/NbSe<sub>2</sub> composite is far from the conventional BCS superconductivity. It suggests that the Weyl semimetal/superconductor composite can have giant proximity effect, resulting in the stable bulk superconductivity in a composite with sizable volume fraction of non-superconducting Weyl semimetals. The giant proximity effect in Weyl semimetal/superconductor interface can have a platform to investigate the proximity induced Weyl semimetallic superconducting states.

*KEYWORDS : NbP, NbSe<sub>2</sub>, Superconductivity, bulk composite, Weyl semimetal.*

<sup>†</sup>Present address : Helmholtzstraße 20, IFW-Dresden, 01069 Dresden, Germany

\*Correspondence should be addressed to J.S.R. ([jsrhyee@khu.ac.kr](mailto:jsrhyee@khu.ac.kr))

## Introduction

Since the discovery of topological insulator, the search on the various topological insulators such as topological crystalline insulator<sup>1</sup>, topological Anderson insulator<sup>2,3</sup>, topological Mott insulator<sup>4</sup>, etc. have been sought out for new state of matter in condensed matter physics. The topological materials have unusual physical properties resulting from massless Dirac fermion, which can control the fascinating transport properties. On the other hand, the detection of surface properties is limited by using the bulk transport measurements because surface to volume ratio is negligible in bulk compounds. Instead, Dirac and Weyl semimetals show topologically protected states in bulk transport properties. A Weyl semimetal is driven by the symmetry breaking either time reversal symmetry or inversion symmetry from Dirac semimetal<sup>5</sup>. Weyl semimetals have a band structure with two Weyl points as one pair, which makes Fermi arcs on a Fermi surface. Weyl points keep opposite chirality and can be either a source or a sink in the form of topological charge, which can be viewed as a monopole. In particular, the bulk properties of Weyl semimetals with the exotic features like chiral anomaly<sup>5-7</sup>, ultra high carrier mobility<sup>8</sup>, and large magnetoresistance<sup>9</sup> are unconventional anomalous transport behavior in terms of robust band topology.

Superconductivity in Weyl semimetals is of great interest but there are not many investigations on the coexistence of bulk superconductivity and a type-I Weyl semimetal (WSM). Type-I Weyl semimetal TaP becomes superconductor under high pressure above 100 GPa, accompanying structural phase transition at 70 GPa<sup>10</sup>. On the other hand, there have been several reports on the coexistence of superconductivity in type-II Weyl semimetals such as MoTe<sub>2</sub> and WTe<sub>2</sub><sup>11-14</sup>. Nevertheless, there are many theoretical suggestions on the existence of Weyl superconductors<sup>15-17</sup>. According to the theoretical prediction, WSM can be a superconducting phase caused by superconducting proximity in heterostructure consisting of a WSM and a superconductor<sup>18</sup>. Experimentally, ion irradiation in NbAs induces breaking the Nb and As bond which leads the natural enrichment of Nb at the surface. Because the excessive Nb becomes superconducting state at  $T_c \sim 3.5$  K, the surface proximity effect makes a superconducting state in Weyl semimetal<sup>19</sup>.

Niobium phosphorus (NbP) which has a noncentrosymmetric structure( $I4_1md$ ) is a representative Weyl semimetal<sup>20-25</sup>. There are 12 Weyl pairs of Weyl nodes in bulk Brillouin zone of NbP based on the first principle calculation<sup>26,27</sup>. It has been shown that the NbP has an ultra-high carrier mobility and chiral anomaly-induced negative magnetoresistance like as typical features of WSM<sup>24,28</sup>.

As a good candidate superconducting material for a heterostructure with NbP, the NbSe<sub>2</sub> exhibits the superconducting transition at  $T_c = 7.2$  K with coexistence of charge density wave at  $T_{CDW} = 33$  K.

It has the similar lattice parameters ( $a=3.44$  and  $c=12.54$ ) with that of NbP ( $a=3.3324$  and  $c=11.3705$ ), which anticipates the coherent interface between NbP and NbSe<sub>2</sub> due to lattice match. Superconductivity also can be induced via the proximity effect, through the interface diffusion of Cooper pairs. NbSe<sub>2</sub> has been known as a Ising type superconductivity<sup>29,30</sup>. Ising superconductivity has the anomalously large in-plane critical magnetic field<sup>31</sup>. The high spin-orbit coupling (SOC) with inversion symmetry breaking locks the pseudospins near K and K' points which are parallel to the c-axis. By the time-reversal symmetry, the pseudospins at K and K' are formed as antiparallel direction with degenerated energy. This unconventional pairing of pseudospins can survive under exceedingly high in-plane magnetic fields comparing with the Pauli limit<sup>32,33</sup>.

Here, we investigated the superconducting properties in NbP/NbSe<sub>2</sub> bulk composite, to explore the proximity induced superconductivity on the NbP, anticipating the coexistence of Weyl semimetallic property as well as the superconducting properties. The magnetic, electronic transport, and heat capacity properties show the robust type-II superconductivity even large volume fraction of non-superconducting NbP (NbP/NbSe<sub>2</sub> = 2 : 1 in molar ratios). In addition, we observed the enhancement of the upper critical field  $H_{c2}$  and the reduction of coherence length  $\xi$  in the composite.

## Results

Fig. 1a shows the X-ray diffraction patterns of the crystalline NbSe<sub>2</sub> (purple) and NbP/NbSe<sub>2</sub> composites with different molar concentrations of NbP/NbSe<sub>2</sub> = 1:1 (red) and 2:1 (black). The reference peaks are also shown for comparison. All labeled diffraction peaks of the grown single crystal of NbSe<sub>2</sub> are aligned along the (00l) peaks, which is indexed by the hexagonal crystalline structure. The diffraction peaks of the composites 1:1 and 2:1 coincide with the standard Bragg peaks with coexisting phases of NbP [PDF#17-0882] and NbSe<sub>2</sub> [PDF#18-0921], indicating the mixed phase composite not a doping. The lattice parameters of NbP phase in the composites are  $a = 3.332 \text{ \AA}$ ,  $c = 11.638 \text{ \AA}$ ,  $V = 126.19 \text{ \AA}^3$  [NbP/NbSe<sub>2</sub> (1:1)] and  $a = 3.326 \text{ \AA}$ ,  $c = 11.408 \text{ \AA}$ ,  $V = 126.19 \text{ \AA}^3$  [NbP/NbSe<sub>2</sub> (2:1)]. The lattice volume of the NbP is not changed for different molar ratio concentrations of NbP/NbSe<sub>2</sub> composites. The lattice parameters of the 2H-NbSe<sub>2</sub> phase on the composites are  $a = 3.450 \text{ \AA}$ ,  $c = 12.530 \text{ \AA}$ ,  $V = 128.36 \text{ \AA}^3$  [NbP/NbSe<sub>2</sub> (1:1)] and  $a = 3.443 \text{ \AA}$ ,  $c = 12.550 \text{ \AA}$ ,  $V = 128.85 \text{ \AA}^3$  [NbP/NbSe<sub>2</sub> (2:1)], respectively. The lattice volume of hexagonal 2H-NbSe<sub>2</sub> little bit increased by increasing the c-axis lattice parameter for increasing NbP concentration, but it is close to the lattice parameters of single crystalline NbSe<sub>2</sub> ( $a = 3.45 \text{ \AA}$  and  $c = 12.544 \text{ \AA}$ ). It shows the stable phase mixing of NbP in NbSe<sub>2</sub> matrix.

The morphologies of the composites show the hexagonal crystal structure of NbSe<sub>2</sub> with the agglomerated NbP particles in Fig. 1b [NbP/NbSe<sub>2</sub> (1:1)] and 1c (2:1), respectively. The typical sizes of crystalline NbSe<sub>2</sub> show tens of  $\mu\text{m}$  scale, while the grain size of NbP have wide range of particle sizes under several  $\mu\text{m}$  scale.

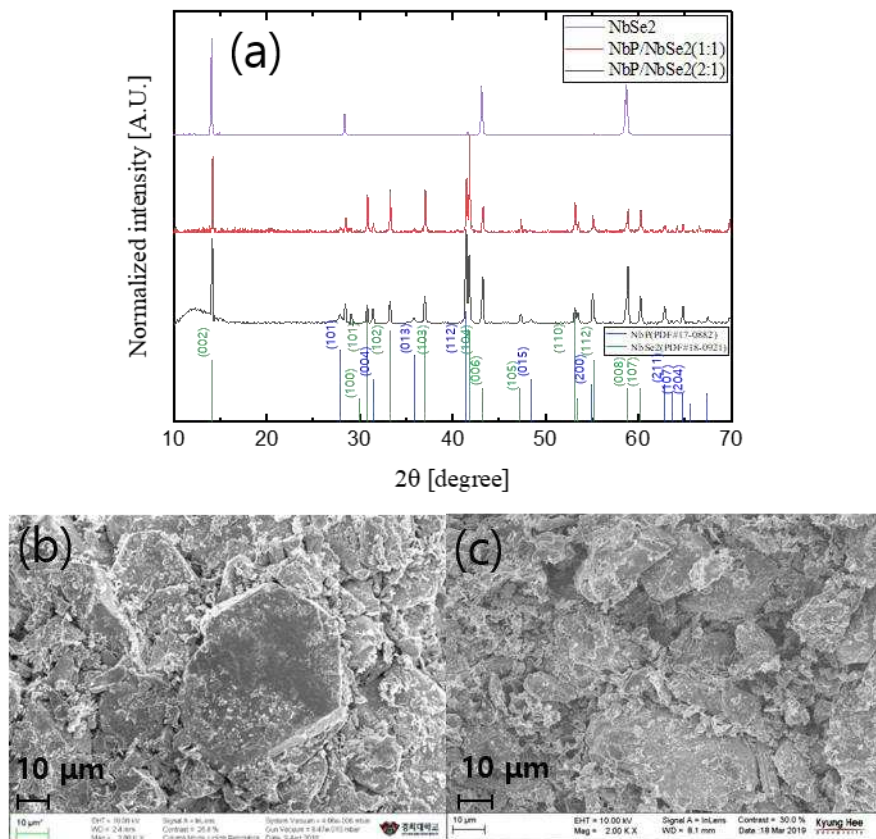


**Figure 1. X-ray diffraction (XRD) patterns and scanning electron microscope (SEM) images.** XRD patterns for the NbSe<sub>2</sub> single crystal (purple), NbP/NbSe<sub>2</sub> composites with molar ratios of 1:1 (red) and 2:1 (black) composites (a). Scanning electron microscope (SEM) images of NbP/NbSe<sub>2</sub> composites with molar ratios of 1:1 (b) and 2:1 (c) molar ratios.

The phase separation of NbP and NbSe<sub>2</sub> can be clearly seen in the elemental mapping from the energy dispersive X-ray spectroscopy (EDX), as presented in Fig. 2. Fig. 2a-d and 2e-h present the elemental mapping on the NbP/NbSe<sub>2</sub> (1:1) and (2:1) composites, respectively. While the Nb is widely distributed as shown in Fig. 2b and 2f, the P and Se elements are clearly distinguishable. For example, Fig. 2a shows clear separation of Se (red dots) and P (green dots) in NbP/NbSe<sub>2</sub> (1:1). Fig. 2e is the EDX mapping of the NbP/NbSe<sub>2</sub> (2:1) composite, showing clear phase separation of Se (pink

dots) and P (bright green dots). Through quantitative analysis of EDX, the concentration of phosphorus in 2:1 sample is larger than those in 1:1 composite.

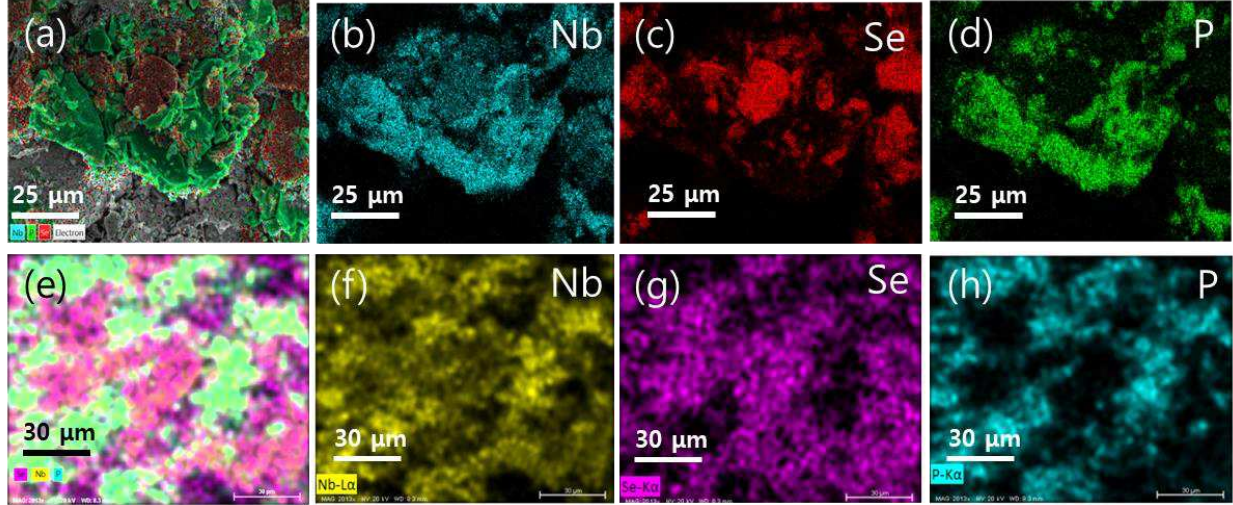


**Figure 2.** Elemental mapping from the energy dispersive X-ray spectroscopy (EDX) of the NbP/NbSe<sub>2</sub> (1:1) (a-d) and NbP/NbSe<sub>2</sub> (2:1) (e-h) composites.

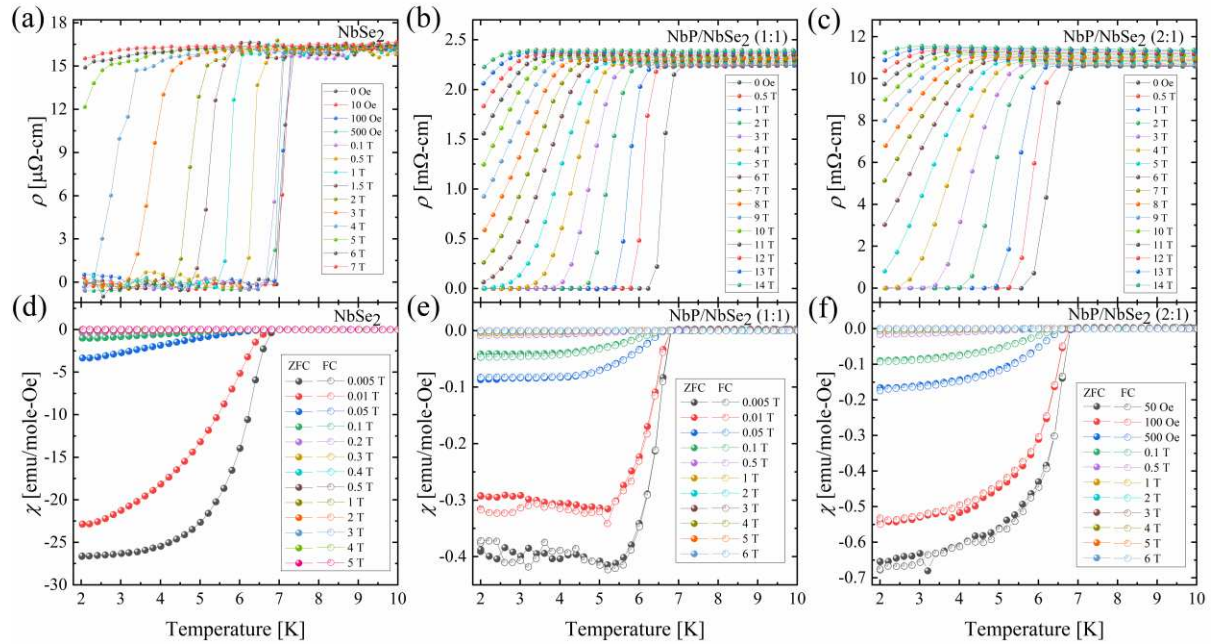


**Figure 3.** Temperature-dependent electrical resistivity  $\rho(T)$  of the NbSe<sub>2</sub> crystal (a), NbP/NbSe<sub>2</sub> (1:1) (b), and NbP/NbSe<sub>2</sub> (2:1) (c). Temperature-dependent magnetic susceptibility  $\chi(T)$  of the NbSe<sub>2</sub> crystal (d), NbP/NbSe<sub>2</sub> (1:1) (e), and NbP/NbSe<sub>2</sub> (2:1) (f).

Fig.s 3 represents the temperature-dependent electrical resistivity  $\rho(T)$  3a-c and magnetization  $M(T)$  3d-f from 2 to 10 K under various applied magnetic fields for the pristine NbSe<sub>2</sub> 3a and 3d, NbP/NbSe<sub>2</sub> (1:1) 3b and 3e, and NbP/NbSe<sub>2</sub> (2:1) 3c and 3f respectively. It is noteworthy that the superconducting transitions are observed in the NbP/NbSe<sub>2</sub> composites even large volume fraction of NbP (2:1). The onset critical temperatures of NbSe<sub>2</sub>, NbP/NbSe<sub>2</sub> (1:1), and NbP/NbSe<sub>2</sub> (2:1) composites are  $T_c = 7.2$  K, 6.9 K, and 6.8 K, respectively. The  $T_c$  (7.2 K) of NbSe<sub>2</sub> is same with the previously reported one<sup>34</sup>. It is surprising because the non-superconducting NbP composite with a sizable phase separation (10~50  $\mu\text{m}$ ) in superconducting NbSe<sub>2</sub> compound show stable superconducting transition. Even though the transition widths of superconducting transition  $\Delta T_c = T_c^{onset} - T_c^{zero}$  are increased with increasing NbP mole fraction, the transition widths  $\Delta T_c$  of NbP/NbSe<sub>2</sub> composites are very sharp comparable with the pristine NbSe<sub>2</sub> crystal;  $\Delta T_c = 0.2$  K (NbSe<sub>2</sub>), 0.6 K (1:1 composite), and 1.2 K (2:1 composite) without magnetic fields.

Fig.s 3d-f shows the magnetic susceptibility as a function of temperature  $\chi(T)$  measured in zero-field cooled (ZFC, closed symbols) and field-cooled (FC, open symbols) cycles under various static magnetic fields for the NbSe<sub>2</sub> and the NbP/NbSe<sub>2</sub> composites (1:1 and 2:1). The onset temperature of the diamagnetic signal is close to  $T_c$  defined in resistivity measurement. The magnetic susceptibilities of the NbP/NbSe<sub>2</sub> composites are weaker than the  $\chi(T)$  value of the NbSe<sub>2</sub> due to the presence of non-magnetic NbP. When we estimate the magnetic susceptibility in the composites, we used the composite density by  $\rho = [\rho_1 V_1 + \rho_2 V_2]/V$ , where  $\rho_{1(2)}$  and  $V_{1(2)}$  are the density and volume of the NbP (NbSe<sub>2</sub>) and  $V$  is the total volume of the sample. Conventional type-II superconductors show strong hysteric behavior of FC and ZFC measurements by strong flux pinning. It is very noteworthy that the  $\chi(T)$  of the NbP/NbSe<sub>2</sub> composites displays strong diamagnetic signal for the FC sequence, which is not significantly different with the ZFC measurement. This strong diamagnetic signal in FC measurement is also exceptional in type II superconductors. The FC and ZFC measurement of NbSe<sub>2</sub> show the paramagnetic signal in FC measurement with strong diamagnetic signal in ZFC measurement, which is conventional behavior. This small differences between ZFC and FC curves in the NbP/NbSe<sub>2</sub> composites indicate a weak flux pinning but strong superconducting state in the composites.

## Discussion

To be a bulk superconductivity in a composite, the Cooper pair should not be scattered near the superconducting/normal metal interface. The only reasonable description on the bulk

superconductivity in the NbP/NbSe<sub>2</sub> composite is the proximity effect between superconducting and normal interface.

From the De Gennes and Meissner theory, the cooper pair electrons in superconductor can penetrate into a normal metal as a characteristic length scale  $\xi_n$  where it is a coherent length of normal metal as a following relation<sup>35,36</sup>:

$$I_c \approx \frac{\pi}{2eR_n} \frac{\Delta_i^2}{kT_c} \frac{d}{\xi_n} e^{-d/\xi_n}$$

where  $R_n$  is the resistance of the junction in its normal state,  $\Delta_i$  is the superconducting energy gap at normal interface,  $T_c$  is the superconducting transition temperature of superconducting side,  $d$  is the thickness of normal layer. In clean limit ( $\xi_s \ll l_n$ ), the characteristic length in normal metal  $\xi_{n,c}$  is presented by  $\xi_{n,c} = \hbar v_n / 2\pi kT$ , where  $v_n$  is the Fermi velocity of normal metal. In dirty limit ( $l_n \ll \xi_s$ ), the characteristic length is given by  $\xi_{n,d} = \sqrt{\hbar v_n l_n / 6\pi kT}$ , where  $l_n$  is the mean free path of normal metal and  $\xi_s$  is the coherence length of superconductor.

Many high temperature superconductors showed that the characteristic length in normal metal by proximity effect is less than 10 Å. For example, the YBa<sub>2</sub>Cu<sub>3</sub>O<sub>7</sub> ( $T_c = 92$  K) and Co-doped PrBa<sub>2</sub>Cu<sub>3</sub>O<sub>7</sub> interface (normal metal) interface exhibits the  $\xi_n = 6$  Å.<sup>37</sup> For  $\xi_n = 5$  μm in NbP/NbSe<sub>2</sub> (2:1) composite, which is necessary for bulk superconductivity in the composite, the Fermi velocity of the normal metal should be  $2.46 \times 10^7$  m/s in a clean limit. The Fermi velocities of the conventional metallic materials are  $1.39 \times 10^6$  m/s (Ag),  $1.52 \times 10^6$  m/s (Cu), and  $2.03 \times 10^6$  m/s (Al), respectively<sup>38</sup>. The Fermi velocity of NbP is estimated by  $3 \times 10^5$  m/s, which is much lower than the expected value in terms of the de Gennes-Meissner criteria<sup>39</sup>. On the other hand, it was observed the giant proximity effect (GPE) in high  $T_c$  cuprate superconductors<sup>40</sup>. The supercurrents can persist in Josephson junctions with high  $T_c$  cuprates as thick as 100 nm~1 μm<sup>41-46</sup>. The de Gennes-Meissner criteria is based on the junctions between conventional s-wave metallic BCS (Bardeen-Cooper-Schrieffer) superconductor and metals. The composites or interfaces comprised with d-wave superconductivity or Weyl semimetals do not follow the de Gennes-Meissner equation. Therefore, the robust bulk superconductivity in NbP/NbSe<sub>2</sub> composite may come from the giant proximity effect in Weyl semimetallic/superconducting bulk composite.

The lower critical field  $H_{c1}$  can be observed in the magnetic field dependent electrical resistivity measurements  $\rho(H)$ , as presented in Fig. 4. The  $H_{c1}$  at 2 K of NbSe<sub>2</sub> crystal shows 4.4 T and the  $H_{c1}$  are increased in the NbP/NbSe<sub>2</sub> composites by about 6 T. The  $H_{c1}$  is decreased with increasing temperatures such as 3.2 T (3 K), 2.4 T (4 K), and 1.5 T (5 K) in NbSe<sub>2</sub> crystal. The decreases of  $H_{c1}$  in the composites are similar to the NbSe<sub>2</sub> crystal; for example, 4 T (3 K), 2.8 T (4 K), and 1.5 T (5 K). On

the other hand, the transition rates of critical field  $H_{c1}$  in the composites are broader than the one of NbSe<sub>2</sub> crystal.

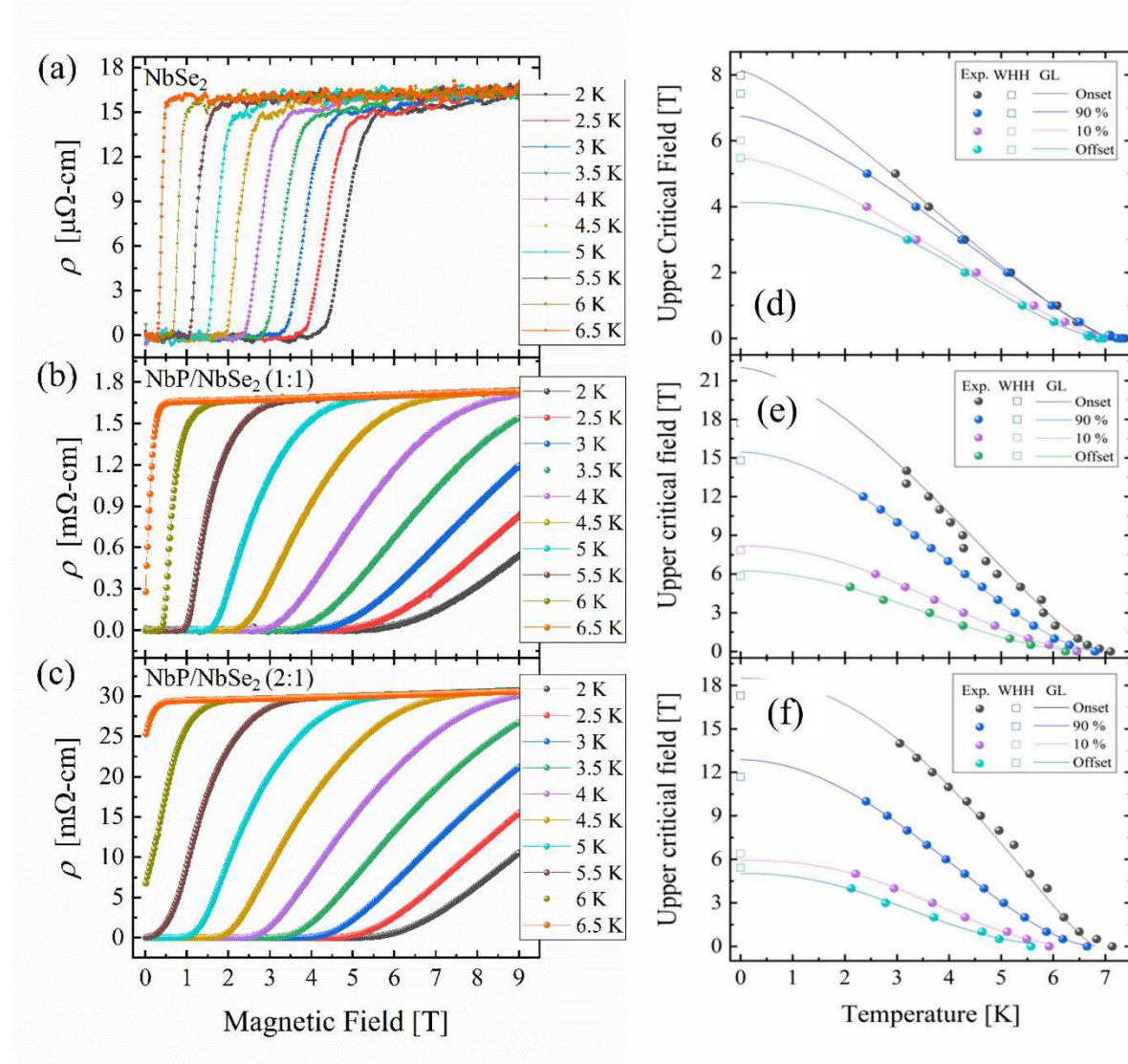


**Figure 4.** Magnetic field dependent isothermal electrical resistivity  $\rho(H)$  at different temperatures and Temperature-dependent upper critical field  $H_{c2}(T)$ .  $\rho(H)$  for the NbSe<sub>2</sub> crystal (a), NbP/NbSe<sub>2</sub> (1:1) (b), and NbP/NbSe<sub>2</sub> (2:1) (c) composites. Temperature-dependent upper critical field  $H_{c2}(T)$  of the NbSe<sub>2</sub> crystal (d), NbP/NbSe<sub>2</sub> (1:1) (e), and NbP/NbSe<sub>2</sub> (2:1) (f) composites. Closed symbols are experimental values from the electrical resistivity and open symbols are  $H_{c2}(0)$  obtained by the WHH formula. Lines are the fitting from the Ginzburg-Landau theory.

From the temperature- and field-dependent electrical resistivity and magnetic susceptibility measurements, we can estimate the superconducting parameters such as the upper critical field  $H_{c2}$ , coherence length  $\xi$ , Ginzburg-Landau parameter  $\kappa$ , and penetration depth  $\lambda$ . The upper critical fields  $H_{c2}(T)$  with temperature are plotted in Fig. 4d-f. Black, blue, purple, and sky-blue symbols represent the  $H_{c2}(T)$  values obtained from the normal-superconducting onset, 90 % and 10 % points from the onset, and zero-resistivity offset points, respectively. Lines are theoretical fitting with the Ginzburg-Landau (GL) equation  $H_{c2}(T)=H_{c2}(0)[1-(T/T_c)]^2$ , which is well fitted with the experimental data. The zero-temperature limit of upper critical field  $H_{c2}(0)$  can be estimated by the GL equation. For example, the  $H_{c2}(0)$ s of the samples are 8 T for NbSe<sub>2</sub>, 22 T for NbP/NbSe<sub>2</sub> (1:1), and 18.5 T for NbP/NbSe<sub>2</sub> (2:1) composites, respectively, from the onset point criteria. It is known that the NbSe<sub>2</sub> is an Ising type superconductivity with strong anisotropic  $H_{c2}(0)$ <sup>47</sup>.

The low temperature upper critical field of the NbSe<sub>2</sub> showed 14 T for along the in-plane and 4 T for the out-of-plane direction<sup>48</sup>. Also, other reports presented the  $H_{c2, //}(0) = 8$  T and  $H_{c2, \perp}(0) = 2$  T for in-plane and out-of-plane direction, respectively<sup>49</sup>. It indicates that the  $H_{c2}(0)$  depends on the sample conditions and  $H_{c2}(0) = 8$  T is the reasonable value along the in-plane upper critical field. It is noteworthy that the non-magnetic NbP composites NbP/NbSe<sub>2</sub> show exceeding value of the  $H_{c2}(0) = 14$  T for the in-plane direction of NbSe<sub>2</sub> even in polycrystal and composite samples. It is very exceptional because non-superconducting composite should degrade the superconductivity.

The  $H_{c2}(0)$  can also be obtained from the Werthamer-Helfand-Hohenberg (WHH) formula, given by  $H_{c2}(0) = -0.693T_c(dH_{c2}/dT)|_{T=T_c}$ <sup>48,50</sup>. The  $H_{c2}(0)$  from the WHH formula is little bit different from the values obtained by the GL theory. Table 1 presents the comparison of the  $H_{c2}(0)$  values obtained from the GL theory and WHH formula. While the  $H_{c2}(0)$  values from the onset points by WHH formula are little bit lower than the values by the GL theory, the  $H_{c2}(0)$  values from the offset points are similar with each other between WHH and GL formulars.

According to the Ginzburg-Landau theory, the  $H_{c2}(0)$  is related with the superconducting coherence length  $\xi$  given by  $H_{c2}(0) = \Phi_0/2\pi\xi^2$ . The coherence lengths at zero temperature also evaluated in Table 1. The coherence length of NbSe<sub>2</sub> crystal is about 6.4 nm. Previous reports evaluated the coherence lengths by  $\xi_c(0) = 2.4$  nm and  $\xi_{ab}(0) = 7.9$  nm along the c-axis and ab-plane, respectively and other reports presented the  $\xi = 5.8$  nm<sup>34,51</sup>. So, the obtained  $\xi = 6.4$  nm is not far from the previous reported ones. The coherence lengths of the NbP/NbSe<sub>2</sub> composites are decreased comparing with the pristine NbSe<sub>2</sub> crystal such as 3.87 nm for NbP/NbSe<sub>2</sub> (1:1) and 4.22 nm for NbP/NbSe<sub>2</sub> (2:1) composites, respectively from the onset points and GL theory reference. On the other hand, the coherence lengths of the NbP/NbSe<sub>2</sub> composites from the offset points are not

significantly decreased with the pristine NbSe<sub>2</sub> such as 8.93 nm for NbSe<sub>2</sub>, 7.3 nm for NbP/NbSe<sub>2</sub> (1:1) and 8.09 nm for NbP/NbSe<sub>2</sub> (2:1) composites, respectively. It is also surprising that the stable bulk superconductivity in the NbP/NbSe<sub>2</sub> composites even though the coherence length is much shorter than the  $\mu\text{m}$  scale mean grain size of NbP. Therefore, the length scale of proximity effect may not be related with the coherence length.

		NbP/NbSe <sub>2</sub>		NbSe <sub>2</sub>	
WHH		1:1	2:1		
$H_{c2}(0)$ [T]	On-set	17.7	17.30	7.89	
	Off-set	5.84	5.43	5.48	
$\zeta$ [nm]	On-set	4.32	4.36	6.43	
	Off-set	7.51	7.78	7.75	
GL		1:1	2:1		
$H_{c2}(0)$ [T]	On-set	22.0	18.5	8.13	
	Off-set	6.25	5.03	4.13	
$\zeta$ [nm]	On-set	3.87	4.22	6.37	
	Off-set	7.30	8.09	8.93	
Abrikosov	$\kappa$	172.7	66.9	27.54	
	$\lambda$ [nm]	668.35	282.32	175.43	
		1:1	2:1	This work	Ref.[34]
$\gamma$ [mJ mol <sup>-1</sup> K <sup>-2</sup> ]		12.0	19.36	18.0	17.4
$\beta$ [mJ mol <sup>-1</sup> K <sup>-4</sup> ]		0.475	0.616	0.603	0.56
$\theta_D$ [K]		274	281	234	218
$\lambda_{el-ph}$		0.738	0.724	0.793	0.81
$\Delta C_e/\gamma T_c$		1.83	1.62	2.03	2.04
$\alpha$		2.01	1.91	2.07	-

**Table 1. Superconducting parameters of the NbSe<sub>2</sub> crystal, NbP/NbSe<sub>2</sub> (1:1), and NbP/NbSe<sub>2</sub> (2:1) composites.** Zero-temperature limit of upper critical field  $H_{c2}(0)$ , coherence length  $\zeta$ , Ginzburg-Landau parameter  $\kappa$ , and penetration depth  $\lambda$ , obtained by the Werthamer-Helfand-Hohenberg (WHH) formula, Ginzburg-Landau (GL), and Abrikosov theory. Sommerfeld coefficient  $\gamma$ , phonon coefficient  $\beta$ , Debye temperature  $\theta_D$ , electron-phonon coupling constant  $\lambda_{el-ph}$ , specific heat jump  $\Delta C_e/\gamma T_c$ , and superconducting gap parameter  $\alpha=\Delta(0)/k_B T_c$  on the NbSe<sub>2</sub> crystal and NbP/NbSe<sub>2</sub> composites.

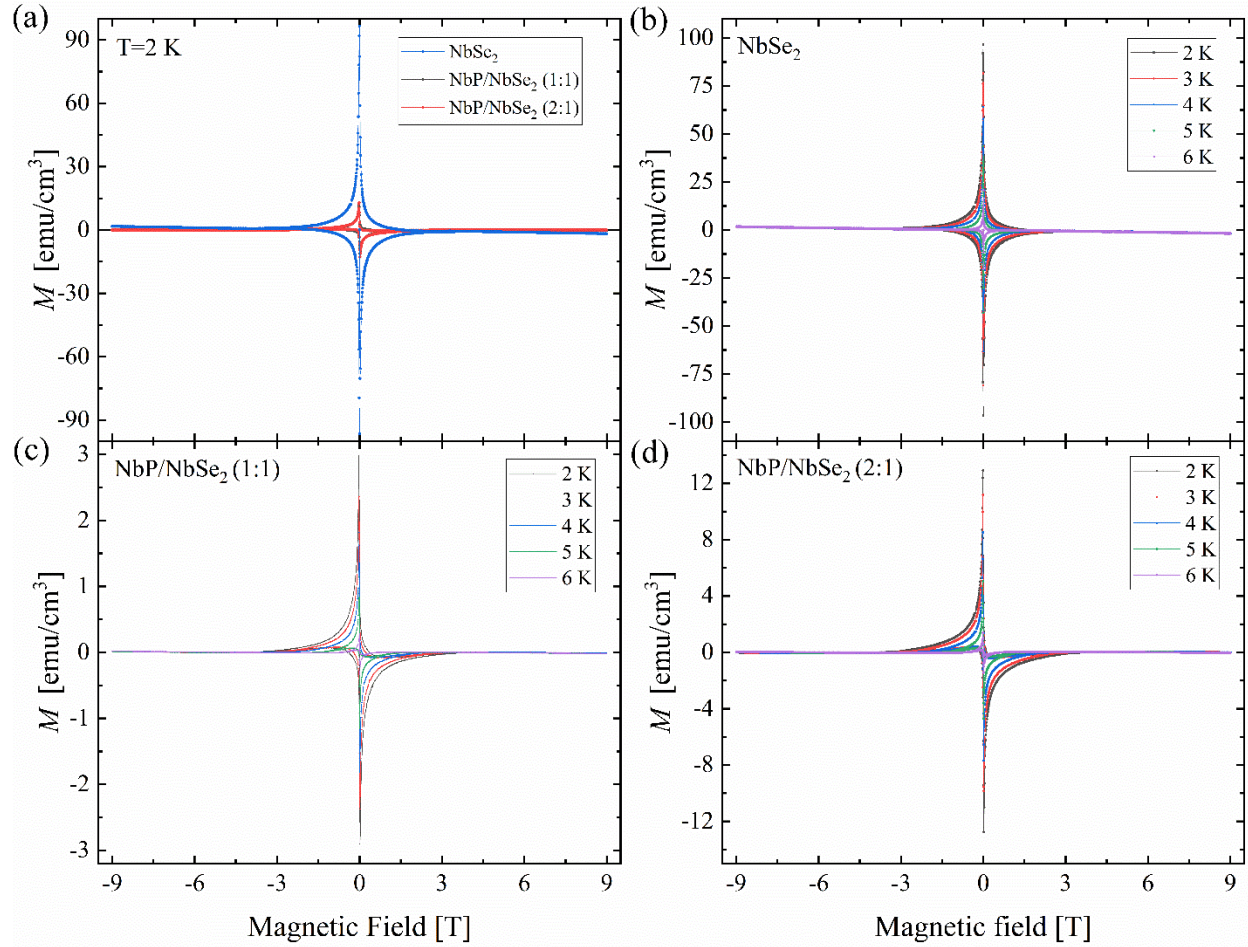


**Figure 5. Isothermal magnetic hysteresis** of the NbSe<sub>2</sub> crystal and composites at T = 2 K (a), M(H) hysteresis of NbSe<sub>2</sub> (b), NbP/NbSe<sub>2</sub> (1:1) (c), and NbP/NbSe<sub>2</sub> (2:1) (d) composites at different temperatures, as indicated.

In addition, the magnetic-hysteresis loops within an applied magnetic field range of  $\pm 9$  T for all the samples at 2 K is illustrated in Fig. 5a. As expected, the magnetic hysteresis of NbSe<sub>2</sub> crystal shows conventional type-II superconducting diamond-like loop. The magnetization of the NbP/NbSe<sub>2</sub> composites are decreased by one order of magnitude or more. Fig. 5b, c, and d present the magnetic hysteresis loop of the NbSe<sub>2</sub> and NbP/NbSe<sub>2</sub> composites [(1:1) and (2:1)] at several temperature below  $T_c$ , as indicated.

It is noteworthy that the magnetic hysteresis curves of the NbP/NbSe<sub>2</sub> composites show asymmetric behavior. It implies that the entrance of vortex to the sample during the increase of magnetic field needs more stronger field energy than those of exit of the vortex from the sample during the decrease of magnetic field. The asymmetric  $M(H)$  curves in the increasing and decreasing

field are originated from the bulk pinning and surface barrier effect in a mixed bulk composite<sup>52</sup>. The presence of the non-superconducting NbP phase in the composites would yield complex pinning mechanism in mixed bulk composites at low magnetic fields. When the contribution of the bulk pinning is dominant compared to the surface pinning, the  $M(H)$  curves becomes symmetric<sup>53</sup>. It is known that even clean NbSe<sub>2</sub> single crystal, there exist significant surface barrier effect<sup>54,55</sup>. On the other hand, this NbSe<sub>2</sub> crystal shows stable symmetric  $M(H)$  hysteresis loop, indicating the stable bulk pinning effect. In some cases, the significant asymmetric  $M(H)$  hysteresis loop has been reported in small doped NbSe<sub>2</sub> single crystal<sup>56</sup>. Therefore, it is not surprising that the significant  $M(H)$  hysteresis loop in NbP/NbSe<sub>2</sub> bulk composites.

According to the Abrikosov theory, the  $M(T, H)$  is expressed by<sup>57</sup>

$$M(H, T) = \frac{H_{c2}(T) - H}{4\pi\beta_A(2\kappa^2 - 1)}$$

where  $\beta_A$  is a constant depending on the vortex arrangement ( $\beta_A = 1.16$  for triangular lattice and 1.18 for square vortex),  $\kappa = \lambda/\xi$  is the Ginzburg-Landau (GL) parameter, and  $\lambda$  is a penetration depth. The field derivative of magnetization near  $H_{c2}$  region can give rise to the Ginzburg-Landau parameter. The GL parameters and penetration depths are presented in Table 1 from the Abrikosov theory. The penetration depths are calculated using the coherence length obtained by the GL theory. The GL parameter of pristine NbSe<sub>2</sub> shows 27.54 which is not significantly different from the ones of previous report. For example, anisotropic GL parameter of NbSe<sub>2</sub> crystal reported<sup>51</sup>  $\kappa_{\perp} = 11$  and  $\kappa_{\parallel} = 29$  and  $\kappa = 33$ <sup>34</sup>. The GL parameters on the composites are significantly enhanced such as 172.5 [NbP/NbSe<sub>2</sub> (1:1)] and 66.9 [NbP/NbSe<sub>2</sub> (2:1)]. This large values of  $\kappa$  are comparable with those of the high temperature superconductors<sup>58</sup>. Because of significant increase of GL parameter in composites, the penetration depths are also significantly increased.

From the magnetic hysteresis measurements, we can obtain the critical current density  $J_c$  as a function of magnetic field, as presented in Fig. 6a-c. The  $J_c$  is estimated from the Bean model given by the relation;  $J_c = 20\Delta M/a(1 - \frac{a}{3b})$ , where  $a$  and  $b$  are the width and length of the sample ( $a < b$ ) and  $\Delta M = M_{\uparrow}(H) - M_{\downarrow}(H)$ <sup>59</sup>. The critical current density of NbSe<sub>2</sub> crystal reaches up to  $1.6 \times 10^4$  A/cm<sup>2</sup>, which is one or two order magnitude larger than the previously reported NbSe<sub>2</sub> crystal<sup>60</sup>  $(1.0 \sim 4.0) \times 10^2$  A/cm<sup>2</sup>, on the other hand one order of magnitude smaller than the Cr-doped NbSe<sub>2</sub> crystal<sup>56</sup>.  $(2.0 \sim 4.0) \times 10^5$  A/cm<sup>2</sup>. The critical current density strongly depends on the sample quality and disorder giving rise to strong or weak flux pinning. The Cr-doped NbSe<sub>2</sub> crystal exhibited both the strong bulk point flux pinning and surface pinning. The  $J_c$  values of the composites are decreased

comparing with the pristine compound such that 500 A/cm<sup>2</sup> and 1900 A/cm<sup>2</sup> for NbP/NbSe<sub>2</sub> (1:1) and (2:1) composites, respectively. Even though the  $J_c$  values are decreased in the composites, it is surprising that the large amount of non-magnetic NbP composite exhibits large critical current density comparable with the previously reported NbSe<sub>2</sub> crystal.

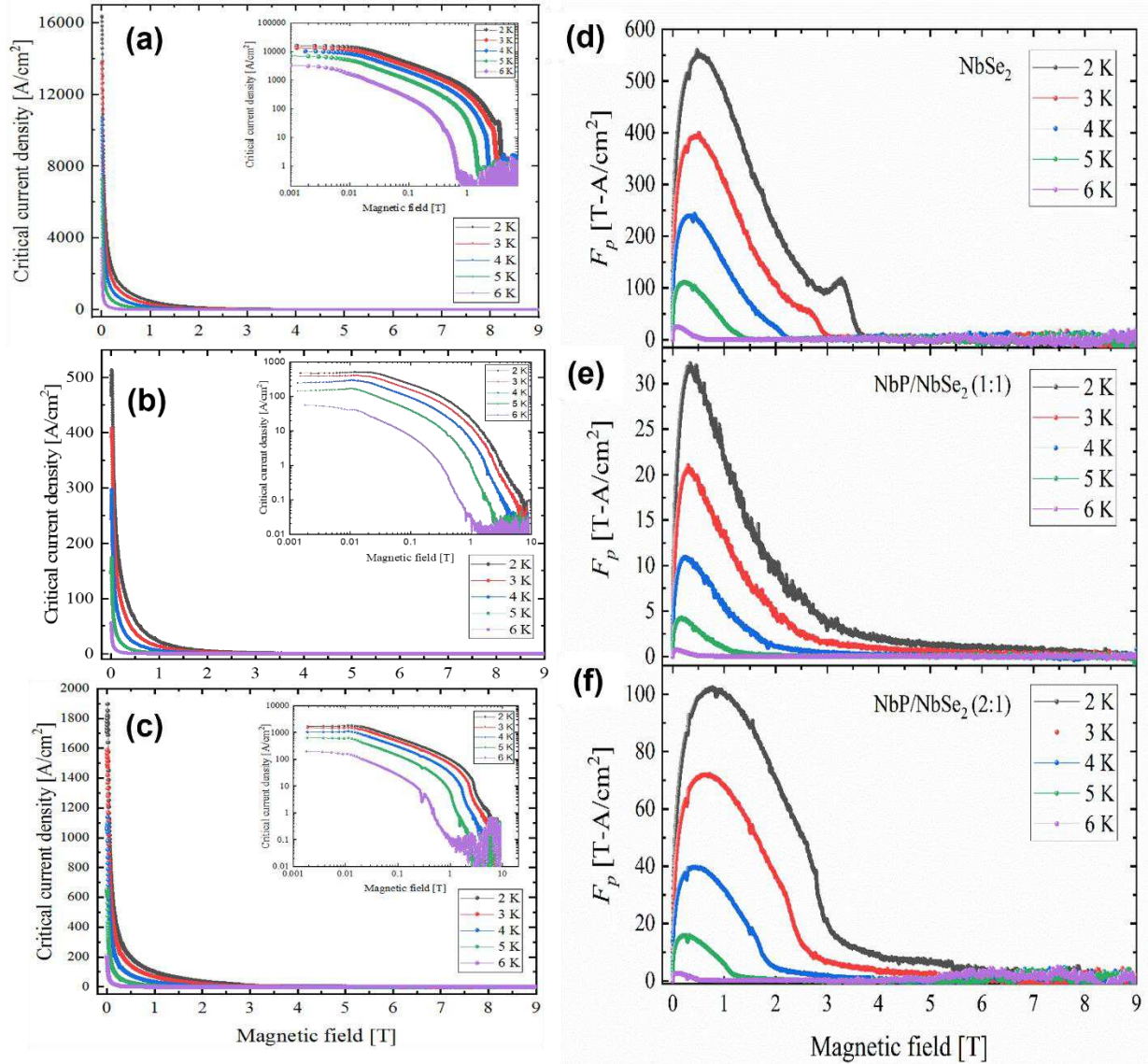


**Figure 6. Isothermal critical current density  $J_c$  and Isothermal pinning force  $F_p$  with magnetic field  $H$  of the NbSe<sub>2</sub> crystal (a) and composites of NbP/NbSe<sub>2</sub> (1:1) (b), and NbP/NbSe<sub>2</sub> (2:1) (c) at various temperature, as indicated. Insets are the log-log scale of the  $J_c(H)$  curves. Isothermal pinning force  $F_p$  with magnetic field  $H$  of the NbSe<sub>2</sub> crystal (d) and composites of NbP/NbSe<sub>2</sub> (1:1) (e), and NbP/NbSe<sub>2</sub> (2:1) (f) at various temperature, as indicated.**

When we plot the log-log scale of the critical current density with magnetic field  $J_c(H)$  as depicted in the insets of Fig. 6a-c, the field dependent behavior shows the saturation at low magnetic fields and rapidly decreasing at high magnetic fields, indicating the formation of vortex bundle and vortex melting at high magnetic fields. It indicates the vortex dynamics on the NbP/NbSe<sub>2</sub> composites is not significantly different with the pristine NbSe<sub>2</sub> crystal.

The vortex pinning force is presented in Fig. 6d-f, obtained by the  $F_p = \mu_0 H \times J_c$ . The vortex competes with the Lorentz force  $F_L = I \times H$  and pinning force. When the Lorentz force is balanced with the pinning force, the vortices are pinned in pinning sites. At low magnetic fields, vortices enter in the bulk of the sample and increases the pinning force with increasing magnetic field. For high magnetic fields, vortices become melting state resulting in the weakening of pinning force with increasing magnetic field. The strongest pinning force is observed near 0.5 Tesla for the compounds of NbSe<sub>2</sub> and their NbP composites. The pinning forces are decreased with increasing temperatures due to thermal fluctuation. There is a pinning force anomaly near 3.3 T for NbSe<sub>2</sub> at T = 2 K. That anomalous pinning force region is also observed in the Cr-doped NbSe<sub>2</sub> crystal, which is described from the effective disorder of the vortex lattice due to the weak pinning potential called plastic deformation of soft flux line lattice<sup>56,61</sup>.

The vortex anomaly is weakened for increasing temperature in NbSe<sub>2</sub>. While the vortex melting is typical in the NbP/NbSe<sub>2</sub> (1:1) composite for decreasing the pinning force with increasing magnetic field, those of NbP/NbSe<sub>2</sub> (2:1) show an abrupt decrease of pinning force near 3 T at 2 K. The abrupt change in the field range may be associated with the vortex breakdown due to abrupt vortex melting. It is also noteworthy that strong pinning force in the composite indicates the strong pinning potential in the NbP/NbSe<sub>2</sub> composite in spite of the non-superconducting NbP composite with large amount of volume fraction.

The superconducting transitions are also observed in specific heat jump near  $T_c$ . Figs 7a~c depict the temperature-dependent specific heat divided by temperature  $C_p/T$  for NbSe<sub>2</sub>, NbP/NbSe<sub>2</sub> (1:1), and NbP/NbSe<sub>2</sub> (2:1) composite samples under static fields as indicated. The specific heat jump near  $T_c$  on the composites shows bulk superconductivity. To derive the electronic and lattice contributions of the specific heat, we fitted the  $C_p/T$  as a function of temperature  $C_p/T = \gamma + \beta T^2$  for normal state under high magnetic fields. From the fitting of normal state specific heat (red lines in Fig. 7), we obtain the Sommerfeld coefficient  $\gamma$  and phonon coefficient  $\beta$ , as presented in Table 1. From the Debye model, we can estimate the Debye temperature  $\theta_D$  by the relation:  $\beta = 12\pi^4 N k_B / 5\theta_D^3$ . The Sommerfeld coefficients of the composites are not changed with the one or pristine compound;  $\gamma = 18 \text{ mJ mol}^{-1} \text{ K}^{-2}$  (NbSe<sub>2</sub>),  $12 \text{ mJ mol}^{-1} \text{ K}^{-2}$  [NbP/NbSe<sub>2</sub> (1:1)], and  $19.4 \text{ mJ mol}^{-1}$

$K^{-2}$  [NbP/NbSe<sub>2</sub> (1:1)], implying the electronic density of state is not changed in the composite. On the other hand, the Debye temperatures are little bit increased in the NbP/NbSe<sub>2</sub> composites comparing with the pristine NbSe<sub>2</sub> crystal; for example, 274 K for (1:1) and 281 for (2:1) NbP/NbSe<sub>2</sub> composites while 220~234 K for NbSe<sub>2</sub> crystal.

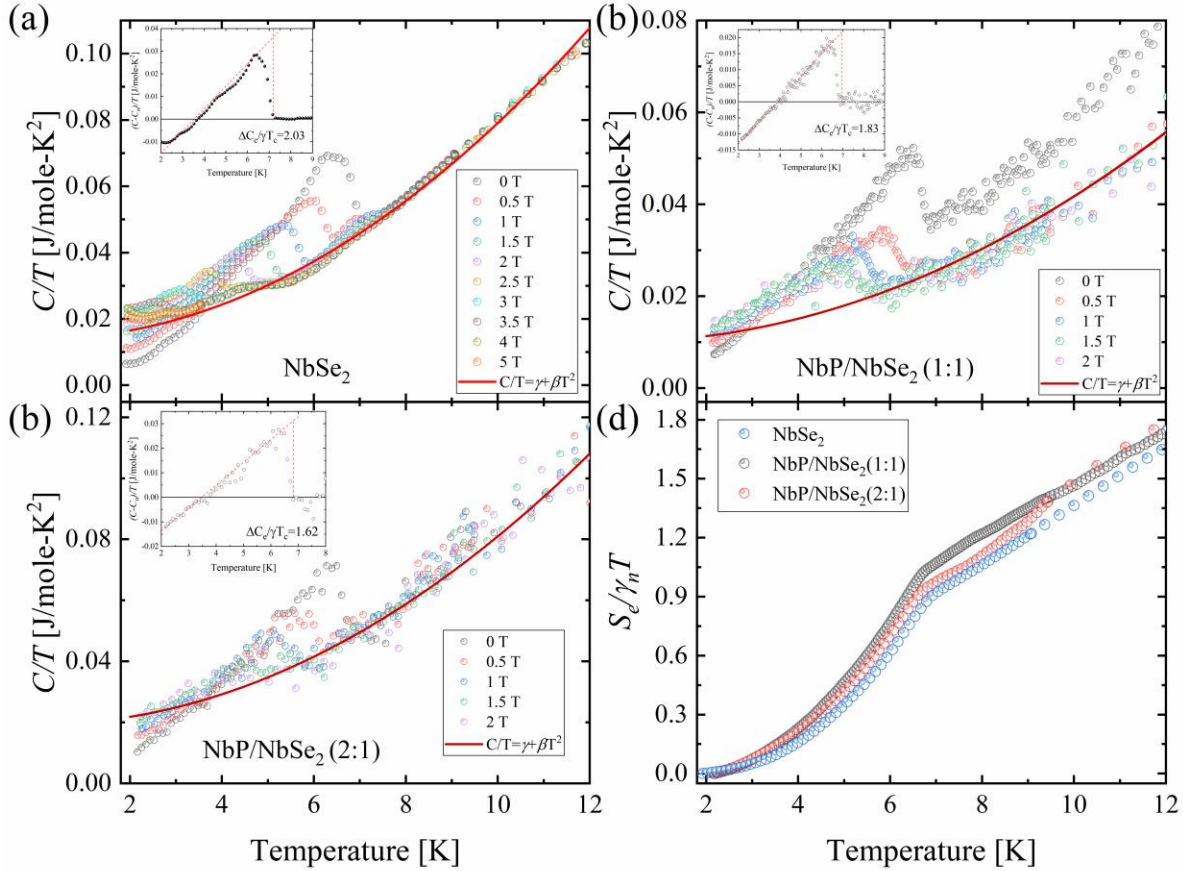


**Figure 7. Temperature-dependent specific heat  $C_p$  divided by temperature  $C_p/T$  of the NbSe<sub>2</sub> crystal (a) and composites of NbP/NbSe<sub>2</sub>(1:1)(b), and NbP/NbSe<sub>2</sub>(2:1)(c) at various MFs (d) Electronic entropy  $S_e$  scaled by the Sommerfeld coefficient  $\gamma_n$  and temperature  $T(S_e/\gamma_n T)$  for  $H=0$ . Insets of (a)~(c) depict the SC specific heat divided by temperature  $(C - C_n)/T$  and estimation of specific heat jump (red dotted line).**

From the Debye temperature  $\theta_D$ , we can obtain the electron-phonon coupling constant  $\lambda_{el-ph}$ , which is important parameter in Bardeen-Cooper-Schrieffer (BCS) superconductors. The electron-phonon coupling constants are calculated to be 0.793, 0.738 and 0.724 using the McMillan formula<sup>62</sup>:

$$\lambda_{el-ph} = \frac{1.04 + \mu^* \ln\left(\frac{\theta_D}{1.45T_c}\right)}{(1 - 0.62\mu^*) \ln\left(\frac{\theta_D}{1.45T_c}\right) - 1.04}$$

where  $\mu^*$  is the pseudo-Coulomb potential and is set to be 0.2, which is a conventional value in BCS superconductor. The obtained values of  $\lambda_{el-ph}$  of all samples suggest intermediate coupled superconductors<sup>57</sup> and the coupling constant of composites are comparable or little bit smaller than pristine NbSe<sub>2</sub>. In spite of non-magnetic NbP composite, it shows the comparable values of electron-phonon coupling constant with the pristine NbSe<sub>2</sub> crystal.

The insets of Figs 7a~c show the superconducting contribution to the specific heat divided by  $T$ ;  $(C-C_n)/T$  by subtracting the normal state specific heat  $C_n$  from the total specific heat. The plot of  $(C-C_n)/T$  versus  $T$  shows the lambda-type specific heat jump  $\Delta C_e$  at  $T_c$ . From the BCS theory, the specific heat jump, defined by  $\Delta C_e/\gamma T_c$  is 1.43 for weak coupling limit. We estimated the  $\Delta C_e/\gamma T_c$  values as 2.03 [NbSe<sub>2</sub>], 1.83 [NbP/NbSe<sub>2</sub> (1:1)], and 1.62 [NbP/NbSe<sub>2</sub> (2:1)], respectively. The values are higher than those of BCS weak coupling limit (1.43) and are decreased with the increase of NbP concentration in the composites. According to the  $\alpha$ -model derived from BCS theory, we can roughly estimate the entropy  $S$  by subtracting the phonon contribution from the superconducting specific heat and using the following relation<sup>63,64</sup>.

$$\frac{\Delta C_{el}}{\gamma_n T_c} = t \frac{d}{dt} \left( \frac{S}{\gamma_n T_c} \right)$$

where  $t = T/T_c$  is the reduced temperature. The calculated electronic entropy scaled by the Sommerfeld coefficient and temperature  $S_e/\gamma_n T$  is plotted in Fig. 7d. The electronic entropy is monotonically decreased with decreasing temperature until  $T_c$  and is exponentially decreased below  $T_c$ . The significant reduction of entropy below  $T_c$  is consistent with the condensation of super-electrons, which decreases entropy.

From the  $\alpha$ -model, the superconducting gap can be measured from the relation<sup>64</sup>:

$$\frac{\Delta C_{el}}{\gamma_n T_c} = 1.426 \left( \frac{\alpha}{\alpha_{BCS}} \right)^2$$

where the  $\alpha$  is the zero-temperature superconducting energy gap scaled by  $k_B T_c$  ( $\Delta(0)/k_B T_c$ ) and  $\alpha_{BCS} = 1.764$ . By using the superconducting specific heat jump, the scaled zero-temperature superconducting energy gaps ( $\alpha$ -value) are 2.07 for NbSe<sub>2</sub>, 2.01 [NbP/NbSe<sub>2</sub> (1:1)], and 1.97 [NbP/NbSe<sub>2</sub> (2:1)], respectively, which are not sensitive with the NbP composite concentration and

are remarkably similar to the reported ones<sup>65</sup>. The gap parameter  $\alpha$ -value in BCS superconductor is known as  $\alpha_{\text{BCS}} = 1.764$ , so the larger  $\alpha$ -value in NbSe<sub>2</sub> and the composites than  $\alpha_{\text{BCS}}$  indicate that the NbSe<sub>2</sub> and the related NbP/NbSe<sub>2</sub> composites are not simply described by the BCS superconducting mechanism.

## Methods

### Sample preparation

We separately synthesize the polycrystalline samples of NbP and NbSe<sub>2</sub> from the solid-state reaction using the starting elements of Nb (99.8 %, Alpha Aesar, U.S.A.) and P (98.9 %, Alpha Aesar, U.S.A.) powders and Se (99.999 %, Alpha Aesar, U.S.A.) granules. The stoichiometric elements of NbP and NbSe<sub>2</sub> were sealed in evacuated quartz ampoules, respectively and heat treated at 850 °C for 48 h and 850 °C for 96 h, respectively. The polycrystalline samples of NbP and NbSe<sub>2</sub> were pulverized respectively and mixed with molar ratios of NbP/NbSe<sub>2</sub> = 1:1 and 2:1 in an agate mortar. The resulting mixed powders were sintered by hot-press sintering at 640 °C, which is much lower temperature of melting point of the compounds to prevent elemental mixing, under a uniaxial pressure of 50 MPa for 1 h.

### Characterization

Structural and phase characterization of the composites were identified by using X-ray diffractometer (Bruker – AXS) with Cu K $\alpha$  radiation ( $\lambda = 0.1546$  nm). The grain morphology of the composites was analyzed by the energy-dispersive x-ray spectroscopy (EDX) with high-resolution scanning electron microscopy (HR-SEM, MERLIN, Carl Zeiss). The magnetization was measured by the physical property measurement system (PPMS-14 T Dynacool, Quantum Design, U.S.A.) with vibrating sample magnetometer (VSM). The electrical resistivity was measured by the 4-point probe method using the PPMS-14 T Dynacool system. Specific heat was also measured by the PPMS-14 T Dynacool system using the thermal relaxation method.

## References

1. Tanaka, Y., Ren, Z., Sato, T., Nakayama, K., Souma, S., Takahashi, T., Segawa, K. Ando, Y., Experimental realization of a topological crystalline insulator in SnTe, *Nat. Phys.* 8, 800-803; <https://doi.org/10.1038/nphys2442> (2012).
2. Xing, Y., Zhang, L., Wang, J., Topological Anderson insulator phenomena, *Phys. Rev. B.* 84, 035110; [10.1103/PhysRevB.84.035110](https://doi.org/10.1103/PhysRevB.84.035110) (2011).
3. Li, J., Chu, R.-L., Jain, J. K., Shen, S.-Q., Topological Anderson Insulator, *Phys. Rev. Lett.* 102, 136806; <https://doi.org/10.1103/PhysRevLett.102.136806> (2009).
4. Raghu, S., Qi, X.-L., Honerkamp, C., Zhang, S.-C., Topological Mott Insulators, *Phys. Rev. Lett.* 100, 156401; [10.1103/PhysRevLett.100.156401](https://doi.org/10.1103/PhysRevLett.100.156401) (2008).
5. Nielsen, H., Ninomiya, N., The Adler-Bell-Jackiw anomaly and Weyl fermions in a crystal, *Phys. Lett. B.* 130, 389-396; [https://doi.org/10.1016/0370-2693\(83\)91529-0](https://doi.org/10.1016/0370-2693(83)91529-0) (1983).
6. Kim, H.-J., Kim, K.-S., Wang, J. F., Sasaki, M., Satoh, N., Ohnishi, A., Kitaura, M., Yang, M., Li, L., Dirac versus Weyl Fermions in Topological Insulators: Adler-Bell-Jackiw Anomaly in Transport Phenomena, *Phys. Rev. Lett.* 111, 246603; <https://doi.org/10.1103/PhysRevLett.111.246603> (2013).
7. Hirschberger, M., Kushwaha, S., Wang, Z., Gibson, Q., Belvin, C. A., Bernevig, B. A., Cava, R. J., Ong, N. P., The Chiral anomaly and thermopower of Weyl fermions in the half Heusler GdPtBi, *Nat. Mater.* 15, 1161-1165; <https://doi.org/10.1038/nmat4684> (2016).
8. Hu, J., Liu, J. Y., Graf, D., Radmanesh, S. M. A., Adams, D. J., Chuang, A., Wang, Y., Chiorescu, I., Wei, J., Spinu, L., Mao, Z. Q.,  $\pi$  Berry phase and Zeeman splitting of Weyl semimetal TaP, *Sci. Rep.* 6, 18674; [doi: 10.1038/srep18674](https://doi.org/10.1038/srep18674). (2016).
9. Kumar, N., Sun, Y., Xu, N., Manna, K., Yao, M., Süß, V., Leermakers, I., Young, O., Förster, T., Schmidt, M., Borrmann, H., Yan, B., Zeitler, U., Shi, M., Felser, C., Shekhar, C., Extremely high magnetoresistance and conductivity in the type -II Weyl semimetals WP<sub>2</sub> and MoP<sub>2</sub>, *Nat. Commun.* 8, 1642; <https://doi.org/10.1038/s41467-017-01758-z> (2017).
10. Li, Y. et al. Concurrence of superconductivity and structure transition in Weyl semimetal TaP under pressure, *npj Quantum Mater.* 2, 66; <https://doi.org/10.1038/s41535-017-0066-z> (2017).
11. Wang, W., Kim, S., Liu, M., Cevallos, F. A., Cava, R. J., Ong, N. P., Evidence for an edge supercurrent in the Weyl superconductor MoTe<sub>2</sub>, *Science* 368, 534-537; [DOI: 10.1126/science.aaw9270](https://doi.org/10.1126/science.aaw9270) (2020).

12. Chen, F. C. et al. Superconductivity enhancement in the S-doped Weyl semimetal candidate MoTe<sub>2</sub>, *Appl. Phys. Lett.* 108, 162601; <https://doi.org/10.1063/1.4947433> (2016).
13. Guguchia, Z. et al. Signatures of the topological  $s^{+-}$  superconducting order parameter in the type-II Weyl semimetal T<sub>d</sub>-MoTe<sub>2</sub>, *Nat. Commun.* 8, 1082; <https://doi.org/10.1038/s41467-017-01066-6> (2017).
14. Chan, Y. T., Alireza, P. L., Yip, K. Y., Niu, Q., Lai, K. T., Goh, S. K., Nearly isotropic superconductivity in the layered Weyl semimetal WTe<sub>2</sub> at 98.5 kbar, *Phys. Rev. B* 96, 180504(R); [10.1103/PhysRevB.96.180504](https://doi.org/10.1103/PhysRevB.96.180504) (2017).
15. Wang, R., Hao, L., Wang, B., Ting, C. S., Quantum Anomalies in superconducting Weyl metals, *Phys. Rev. B.* 93, 184511; [10.1103/PhysRevB.93.184511](https://doi.org/10.1103/PhysRevB.93.184511) (2016).
16. Zhou, T., Gao, Y., Wang, Z. D., Superconductivity in doped inversion-symmetric Weyl semimetals. *Phys. Rev. B.* 93, 094517; [10.1103/PhysRevB.93.094517](https://doi.org/10.1103/PhysRevB.93.094517) (2016).
17. Hao, L., Ting, C. S., Searching for two-dimensional Weyl superconductors in heterostructures, *Phys. Rev. B.* 95, 064513; [10.1103/PhysRevB.95.064513](https://doi.org/10.1103/PhysRevB.95.064513) (2017).
18. Khanna, U., Kundu, A., Pradhan, S., Rao, S., Proximity-induced superconductivity in Weyl semimetals, *Phys. Rev. B* 90, 195430; [10.1103/PhysRevB.90.195430](https://doi.org/10.1103/PhysRevB.90.195430) (2014).
19. Bachmann, M. D. et al. Inducing superconductivity in Weyl semimetal microstructures by selective ion sputtering, *Sci. Adv.* 3, e1602983; DOI: [10.1126/sciadv.1602983](https://doi.org/10.1126/sciadv.1602983) (2017).
20. Inoue, H., Gyenis, A., Wang, Z., Li, J., Oh, S. W., Jiang, S., Ni, N., Bernevig, B. A., Yazdani, A., Quasiparticle interference of the Fermi arcs and surface-bulk connectivity of a Weyl semimetal, *Science* 351, 1184-1187; DOI: [10.1126/science.aad8766](https://doi.org/10.1126/science.aad8766) (2016).
21. Sergelius, P., Gooth, J., Bäßler, S., Zierold, R., Wiegand, C., Niemann, A., Reith, H., Shekhar, C., Felser, C., Yan, B., Nielsch, K., Berry phase and band structure analysis of the Weyl semimetal NbP, *Sci. Rep.* 6, 33859; <https://doi.org/10.1038/srep33859> (2016).
22. Liu, Z. K., Yang, L. X., Sun, Y., Zhang, T., Peng, H., Yang, H. F., Chen, C., Zhang, Y., Guo, Y. F., Prabhakaran, D., Schmidt, M., Hussain, Z., Mo, S.-K., Felser, C., Yan, B., Chen, Y. L., Evolution of the Fermi surface of Weyl semimetals in the transition metal pnictide family, *Nat. Mater.* 15, 27-31; <https://doi.org/10.1038/nmat4457> (2015).
23. Xu, N., et al. Distinct Evolutions of Weyl Fermion Quasiparticles and Fermi Arcs with Bulk Band Topology in Weyl Semimetals, *Phys. Rev. Lett.* 118, 106406; <https://doi.org/10.1103/PhysRevLett.118.106406> (2017).
24. Shekhar, C., et al. Extremely large magnetoresistance and ultrahigh mobility in the topological Weyl semimetal candidate NbP, *Nat. Phys.* 11, 645-650; <https://doi.org/10.1038/nphys3372> (2015).

25. Gooth, J., et al. Experimental signatures of the mixed axial–gravitational anomaly in the Weyl semimetal NbP, *Nature* 547, 324-327; <https://doi.org/10.1038/nature23005> (2017).
26. Sun, Y., Wu, S.-C., Yan, B., Topological surface states and Fermi arcs of the noncentrosymmetric Weyl semimetals TaAs, TaP, NbAs and NbP, *Phys. Rev. B.* 92, 115428; [10.1103/PhysRevB.92.115428](https://doi.org/10.1103/PhysRevB.92.115428) (2015).
27. Huang, S.-M., Xu, S.-Y., Belopolski, I., Lee, C.-C., Chang, G., Wang, B., Alidoust, N., Bian, B., Neupane, M., Zhang, C., Jia, S., Bansil, A., Lin, H., Hasan, Z. M., A Weyl Fermion semimetal with surface Fermi arcs in the transition metal monopnictide TaAs class, *Nat. Commun.* 6, 7373; <https://doi.org/10.1038/ncomms8373> (2015).
28. Niemann, A. C., Gooth, J., Wu, S.-C., Bler, S., Sergelius, P., Hhne, R., Rellinghaus, B., Shekhar, C., Süß, V., Schmidt, M., Chiral magnetoresistance in the Weyl semimetal NbP, *Sci. Rep.* 7, 43394; <https://doi.org/10.1038/srep43394> (2017).
29. Wickramaratne, D., Khmelevskiy, S., Agterberg, D. F., Mazin, I. I., Ising Superconductivity and Magnetism in NbSe<sub>2</sub>, *Phys. Rev. X* 10, 041003; <https://doi.org/10.1103/PhysRevX.10.041003> (2020).
30. Xing, Y. et al. Ising Superconductivity and Quantum Phase Transition in Macro-Size Monolayer NbSe<sub>2</sub>, *Nano Lett.* 17, 6802-6807; <https://doi.org/10.1021/acs.nanolett.7b03026> (2017).
31. Saito, Y., Nojima, T., Iwasa, Y., Highly crystalline 2D superconductors, *Nat. Rev. Mater.* 2, 16094; <https://doi.org/10.1038/natrevmats.2016.94> (2017).
32. Xi, X., Wang, Z., Zhao, W., Park, J.-H., Law, K. T., Berger, H., Forró, L., Shan, J., Mak, K. F., Ising Pairing in Superconducting NbSe<sub>2</sub> Atomic Layers, *Nat. Phys.* 12, 139; <https://doi.org/10.1038/nphys3538> (2016).
33. Sergio, C., Sinko, M. R., Gopalan, D. P., Sivadas, N., Seyler, K. L., Watanabe, K., Taniguchi, T., Tsen, A. W., Xu, X., Xiao, D., Hunt, B., Tuning Ising Superconductivity with Layer and Spin-Orbit Coupling in Two-Dimensional Transition-Metal Dichalcogenides, *Nat. Commun.* 9, 1427; <https://doi.org/10.1038/s41467-018-03888-4> (2018).
34. Luo, H., Nowak, J. S., Li, J., Tao, J., Klimczuk, T., Cava, R. J., S-Shaped Suppression of the superconducting Transition Temperature in Cu-Intercalated NbSe<sub>2</sub>, *Chem. Mater.* 29, 3704-3712; <https://doi.org/10.1021/acs.chemmater.7b00655> (2017).
35. De Gennes, P. G., Boundary Effects in Superconductors, *Rev. Mod. Phys.* 36, 225; <https://doi.org/10.1103/RevModPhys.36.225> (1964).
36. Meissner, H., Superconductivity of Contacts with Interposed Barriers, *Phys. Rev.* 117 672; <https://doi.org/10.1103/PhysRev.117.672> (1960).

37. Yoshida, J., Recent Progress of High-Temperature Superconductor Josephson Junction Technology for Digital Circuit Applications, *IEICE Trans. Electron.* E83-C, 49-59, (2000).
38. Ashcroft, N. W., Mermin, N. D., *Solid State Physics* (Saunders College Publishing, New York, 1976) Ch. 2, p.38
39. Lee C.-C. et al. Fermi surface interconnectivity and topology in Weyl fermion semimetals TaAs, TaP, NbAs, and NbP, *Phys. Rev. B* 92, 235104; <https://doi.org/10.1103/PhysRevB.92.235104> (2015).
40. Bozovic, I., Logvenov, G., Verhoeven, M. A. J., Caputo, P., Goldobin, E., Beasley, M. R., Giant Proximity Effect in Cuprate Superconductors, *Phys. Rev. Lett.* 93, 157002; [10.1103/PhysRevLett.93.157002](https://doi.org/10.1103/PhysRevLett.93.157002) (2004).
41. Kabasawa U. et al. Electrical Characteristics of  $\text{HoBa}_2\text{Cu}_3\text{O}_{7-x}\text{-La}_{1.5}\text{Ba}_{1.5}\text{Cu}_3\text{O}_{7-y}\text{-HoBa}_2\text{Cu}_3\text{O}_{7-x}$  Junctions with Planar-Type Structures, *Jpn. J. Appl. Phys.* 30, 1670, (1991).
42. Yuasa, R., Nemoto, M., Fujiwara, S., Furukawa, H., Mukaida, H., Tokunaga, S., Nakao, M., Long-range Josephson coupling in planar SNS junctions, *Physica C (Amsterdam)* 185C, 2587; <https://doi.org/10.1103/PhysRevB.78.115413> (1991).
43. Barner J. B. et al. All a-axis oriented  $\text{YBa}_2\text{Cu}_3\text{O}_{7-y}\text{-PrBa}_2\text{Cu}_3\text{O}_{7-z}\text{-YBa}_2\text{Cu}_3\text{O}_{7-y}$  Josephson devices operating at 80 K, *Appl. Phys. Lett.* 59, 742; <https://doi.org/10.1063/1.105330> (1991).
44. Meltzow A. C. et al. Doped-type coplanar junctions in the  $\text{Bi}_2\text{Sr}_2\text{CaCu}_2\text{O}_{8+\delta}$  system, *IEEE Trans. Appl. Supercond.* 7, 2852; [10.1109/77.621880](https://doi.org/10.1109/77.621880) (1997).
45. Decca R. S., et al. Anomalous Proximity Effect in Underdoped  $\text{YBa}_2\text{Cu}_3\text{O}_{6+x}$  Josephson Junctions, *Phys. Rev. Lett.* 85, 3708; <https://doi.org/10.1103/PhysRevLett.85.3708> (2000).
46. Krivoruchko, V. N., Tarenkov, V. Y., Triple -gap superconductivity of  $\text{MgB}_2\text{-(La,Sr)MnO}_3$  Composite, *Phys. Rev. B.* 86, 104502; [10.1103/PhysRevB.86.104502](https://doi.org/10.1103/PhysRevB.86.104502) (2012).
47. Zhou, K., Deng, J., Guo, L., Guo, J., Tunable Superconductivity in 2H-NbSe<sub>2</sub> via In Situ Li Intercalation, *Chin. Phys. Lett.* 37, 097402; (2020).
48. Werthamer, N. R., Helfand, E., Hohenberg, P. C., Temperature and Purity Dependence of the Superconducting Critical Field,  $H_{c2}$ . III. Electron Spin and Spin-Orbit Effects, *Phys. Rev.* 147, 295-302; <https://doi.org/10.1103/PhysRev.147.295> (1966).
49. Morris, R. C., Coleman, R. V., Bhandari, R., Superconductivity and Magnetoresistance in NbSe<sub>2</sub>, *Phys. Rev. B.* 5, 895; <https://doi.org/10.1103/PhysRevB.5.895> (1972).

50. Samuely, P., Szabó, P., Klein, T., Jansen, A. G. M., Marcus, J., Escribe-Filippini, C., Wyder, P., Upper critical field in  $Ba_{1-x}K_xBiO_3$ : Magnetotransport vs. Magnetotunneling, *Europhys. Lett.* 41, 207–212; (1998).
51. Soto, F., Berger, H., Cabo, L., Carballeira, C., Mosqueira, J., Pavuna, D., Toimil, P., Vidal, F., Electric and magnetic characterization of  $NbSe_2$  single crystals: Anisotropic superconducting fluctuations above  $T_c$ , *Physica C* 460-462, 789-790; <https://doi.org/10.1016/j.physc.2007.04.032> (2007).
52. Semenov, S. V., Balaev, D. A., Temperature behavior of the magnetoresistance hysteresis in a granular high-temperature superconductor: Magnetic flux compression in the intergrain medium, *Physica C* 550, 19-26; <https://doi.org/10.1016/j.physc.2018.04.005> (2018).
53. Kim, M.-S., Jung, C. U., Park, M.-S., Lee, S. Y., Kim, K. H. P., Kang, W. N., Lee, S.-I., Prominent bulk pinning effect in the  $MgB_2$  superconductor, *Phys. Rev. B* 64, 012511; <https://doi.org/10.1103/PhysRevB.64.012511> (2001).
54. Bermudez, M. M., Loudon, E. R., Eskildsen, M. R., Dewhurst, C. D., Bekeris, V., Pasquini, G., Metastability and hysteretic vortex pinning near the order-disorder transition in  $NbSe_2$ : Interplay between plastic and elastic energy barriers, *Phys. Rev. B* 95, 104505; <https://doi.org/10.1103/PhysRevB.95.104505> (2017).
55. Mishra, P. K., Ravikumar, G., Rao, T. V. C., Sahni, V. C., Banerjee, S. S., Ramakrishnan, S., Grover, A. K., Higgins, M. J., Surface barrier effect and the crossover in magnetization relaxation in  $2H-NbSe_2$ , *Physica C* 340, 64-70; [https://doi.org/10.1016/S0921-4534\(00\)00369-5](https://doi.org/10.1016/S0921-4534(00)00369-5) (2000).
56. Pervin, R., Krishnan, M., Rana, A. K., Arumugam, S., Shirage, P. M., Effect of Cr atoms in vortex dynamics of  $NbSe_2$  superconductor and study of second magnetization peak effect, *Mater. Res. Express.* 5, 076001; (2018).
57. Doria, M. M., Romaguera, A. R. C., Salem-Sugui, S. Jr., Vanishing of the upper critical field in  $Bi_2Sr_2CaCu_2O_{8+\delta}$  from Landau-Ott scaling, *Phys. Rev. B.* 76, 052054; <https://doi.org/10.1103/PhysRevB.76.052054> (2007).
58. Poole, C. P., Farach, H. A., Creswick, R. J., *Superconductivity* (Academic Press, New York, 1995, chap. 9, p. 271).
59. Bean, C. P., Magnetization of High-Field Superconductors, *Rev. Mod. Phys.* 36, 31–39; <https://doi.org/10.1103/RevModPhys.36.31> (1964).
60. Spiering, G. A. Revolinsky, E., Beerntsen, D. J., Critical currents in superconducting single crystal Niobium Diselenide, *J. Phys. Chem. Solids.* 27, 535-541; [https://doi.org/10.1016/0022-3697\(66\)90197-1](https://doi.org/10.1016/0022-3697(66)90197-1) (1966).
61. Higgins, M. J., Bhattacharya, S., Varieties of dynamics in a disordered flux-line lattice. *Physica C* 257, 232-254; [https://doi.org/10.1016/0921-4534\(95\)00704-0](https://doi.org/10.1016/0921-4534(95)00704-0) (1996).

62. McMillan, W. L., Transition temperature of Strong-Coupled Superconductors, Phys. Rev. 167, 331-344; <https://doi.org/10.1103/PhysRev.167.331> (1968).
63. Singh, D., Barker, J. A. T., Thamizhavel, A., Hillier, A. D., Paul, McK. D., Singh, R. P., Superconducting properties and  $\mu$ SR study of the noncentrosymmetric superconductor Nb<sub>0.5</sub>O<sub>5</sub>, J. Phys. Condens. Matter. 30 075601-075601, (2018).
64. Johnston, D. C., Elaboration of the  $\alpha$ -model derived from the BCS theory of Superconductivity, Supercond. Sci. Technol. 26, 115011; (2013).
65. Huang, C. L., Lin, J.-Y., Chang, Y. T., Sun, C. P., Shen, H. Y., Chou, C. C., Berger, H., Lee, T. K., Yang, H. D., Experimental evidence for a two-gap structure of superconducting NbSe<sub>2</sub>: A specific-heat study in external magnetic fields, Phys. Rev. B. 76, 212504; <https://doi.org/10.1103/PhysRevB.76.212504> (2007).

### **Acknowledgment**

This research was supported by a grant from Kyung Hee University (20171203), Korea and by the National Research Foundation of Korea(NRF) funded by the Ministry of Education, Science and Technology (NRF-2020R1A2C2009353, NRF-2020K1A4A7A02095438). Dr. Omkaram Inturu was supported by the National Research Foundation of Korea(NRF) funded by the Ministry of Education, Science and Technology (NRF-2019H1D3A2A02102233).

### **Author contribution statement**

**Jong-Soo Rhyee**: designed and advised the work, analyze the data, revised the manuscript. **Yejin Lee**: conducted the whole work from experiment, analyze the data, and write a draft. **Omkaram Inturu**: conducting an experiment and revised the manuscript. **Jin Hee Kim**: conducted the experimental work.

### **Additional information**

#### **Declaration of Competing Interest**

The authors declare that they have no known competing financial interests or personal relationships that could have appeared to influence the work reported in this paper.